

**Multiple Andreev reflections in topological Josephson junctions with chiral Majorana modes**Linde A. B. Olde Olthof <sup>1,2,\*</sup>, Stijn R. de Wit <sup>1,\*</sup>, Shu-Ichiro Suzuki <sup>1,3</sup>, Inanc Adagideli <sup>1,4,5</sup>  
Jason W. A. Robinson <sup>2</sup> and Alexander Brinkman <sup>1,†</sup><sup>1</sup>*MESA+ Institute for Nanotechnology, University of Twente, 7500 AE Enschede, The Netherlands*<sup>2</sup>*Department of Materials Science & Metallurgy, University of Cambridge, CB3 0FS Cambridge, United Kingdom*<sup>3</sup>*Department of Applied Physics, Nagoya University, 464-8603 Nagoya, Japan*<sup>4</sup>*Faculty of Engineering and Natural Sciences, Sabanci University, 34956 Istanbul, Turkey*<sup>5</sup>*TÜBİTAK Research Institute for Fundamental Sciences, 41470 Gebze, Turkey*

(Received 16 December 2022; revised 10 March 2023; accepted 18 April 2023; published 18 May 2023)

Andreev bound states (ABSs) occur in Josephson junctions when the total phase of the Andreev and normal reflections is a multiple of  $2\pi$ . In ballistic junctions with an applied voltage bias, a quasiparticle undergoes multiple Andreev reflections before entering the leads, resulting in peaks in the current-voltage  $I(V)$  curve. Here we present a model for a two-dimensional S/TI/MTI/TI/S junction, where S is a superconductor, TI is a topological insulator, and MTI is a magnetic topological insulator barrier. We show that the interplay of broken time-reversal symmetry and topology results in an asymmetric  $I(V)$  curve. Such junctions are predicted to host chiral Majorana modes. We demonstrate that the peak positions in  $I(V)$  are directly linked to ABSs. We use this to show how the angle-resolved  $I(V)$  curve becomes a spectroscopic tool for the chirality and degeneracy of ABSs.

DOI: [10.1103/PhysRevB.107.184510](https://doi.org/10.1103/PhysRevB.107.184510)**I. INTRODUCTION**

Andreev reflection is the conversion of an electron into a hole with opposite spin upon reflecting from a superconductor interface [1]. Andreev bound states (ABSs) arise when a combination of a number of Andreev and normal reflections fulfills the Bohr-Sommerfeld quantization condition in which the total phase adds up to multiples of  $2\pi$ . Renowned examples include bound states that carry the supercurrent between two superconducting leads across a normal metal [2], the Yu-Shiba-Rusinov bound states that involve scattering from a magnetic impurity [3–5], and the Caroli–De Gennes–Matricon bound state in the core of an Abrikosov vortex [6]. Generally, the required phase quantization is fulfilled either by incorporating spin-active scattering with different phases for the reflection of different spins [7–9] or by picking up a phase difference due to an anisotropic order parameter in the superconductor (an unconventional superconductor) [10–12].

At the surface or interface of an unconventional superconductor, surface ABSs at zero energy (relative to the Fermi energy) arise when the phase difference between the energy-dependent Andreev reflection of the electron and hole is  $\pi$ . This has been measured at the surface of a  $45^\circ$  grain boundary junction involving a  $d_{x^2-y^2}$  cuprate superconductor [12] and predicted for the surface of a chiral  $p$ -wave superconductor [13]. Surface ABSs become (chiral) Majorana bound states upon lifting the spin degeneracy by breaking time-reversal symmetry in a topological superconductor [14],

either by a vortex [15] or an external magnetic field [16]. The distinguishing feature of a Majorana bound state is the zero-bias conductance peak in the tunneling conductance [10,17], which is quantized at the value  $2e^2/h$  in the nondegenerate single-mode regime [14,18].

Here, we theoretically study the influence of (chiral) interface ABSs on the current-voltage characteristics of Josephson junctions. Besides a zero-voltage supercurrent, Josephson junctions are characterized by a subgap structure in the finite-bias conductance that arises from multiple Andreev reflections (MARs). In a Josephson junction with a normal metal interlayer (S/N/S), MARs provide peaks at  $2\Delta/n$ , where  $\Delta$  is the superconducting energy gap, and  $n$  is the integer number of times that the electrons or holes traverse the junction before entering the leads [19]. If a topological insulator (TI) interlayer featuring a magnetic topological insulator (MTI) barrier is used instead of a normal metal barrier, the subgap state opens an extra conduction channel and the peaks in a one-dimensional (1D) S/TI/MTI/TI/S junction are located at  $\Delta/n$  [20]. Our work focuses on the two-dimensional (2D) S/TI/MTI/TI/S junction, where we consider the charge transport through the surface of a three-dimensional TI. The aforementioned S/N/S and 1D S/TI/MTI/TI/S junctions are limiting cases.

The approach is as follows: we first deconstruct the S/TI/MTI/TI/S junction into two half-junctions: S/TI/MTI and MTI/TI/S. We write down the Hamiltonian in Sec. II and use it to study the topological invariant in Sec. III. We investigate the existence and energy dependence of ABSs in S/TI/MTI and MTI/TI/S half-junctions in Sec. IV. We couple the two half-junctions into an S/TI/MTI/TI/S junction and calculate the  $I(V)$  spectrum in Sec. V. In Sec. VI, we

\*These authors contributed equally to this work.

†a.brinkman@utwente.nl

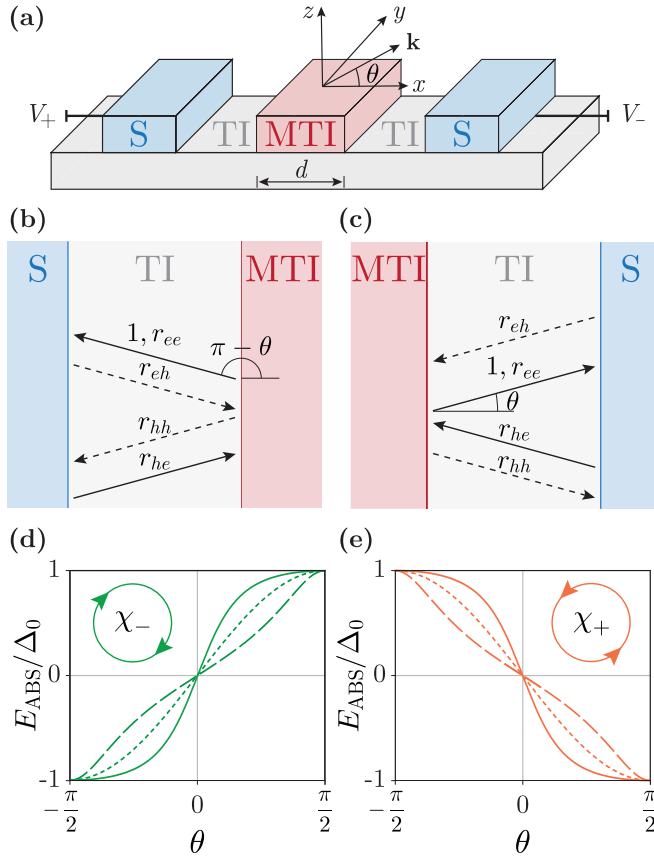


FIG. 1. (a) Schematic illustration of the S/TI/MTI/TI/S junction setup, where Andreev reflection occurs in the two TI regions which are coupled via a scattering region MTI of width  $d$ . (b) and (c) The top view of the S/TI/MTI/TI/S junction split in two half-junctions S/TI/MTI and MTI/TI/S, where normal ( $r_{ee}$ ,  $r_{hh}$ ) and Andreev ( $r_{eh}$ ,  $r_{he}$ ) reflections occur.  $\tan \theta = k_y/k_x$ , with  $k_x$  and  $k_y$  being the components of the plane-wave momenta. (d) and (e) The two half-junctions host chiral Majorana modes of opposite chirality  $\chi_{\mp}$ . Their normalized bound-state levels  $E_{\text{ABS}}/\Delta_0$  as a function of the incident angle  $\theta$  are shown for (d) an MTI/TI/S junction and (e) an S/TI/MTI junction. The dashed, dotted, and solid lines correspond to  $\mu_{\text{TI}}/m_z = 0.5, 1, \text{ and } 2$ , respectively. The other parameters are  $m_z = 300\Delta_0$ ,  $\mu_{\text{MTI}} = 0$ , and  $\mu_{\text{TI}} = \mu_{\text{S}}$ .

show that the features in  $I(V)$  are asymmetric and are directly linked to the presence of ABSs. We show how  $I(V)$  changes for lateral junctions and nanowires in Sec. VII. Finally, we generalize our results for nontopological systems and discuss how angle-resolved MARs can become a spectroscopic tool for the chiral nature and degeneracy of ABSs in Sec. VIII.

## II. HAMILTONIAN

We present a generalized model for a 2D S/TI/MTI/TI/S Josephson junction, as illustrated in Fig. 1(a). We note that the S is an  $s$ -wave superconductor, the MTI is a magnetic TI in which the magnetism is either intrinsic or induced (a ferromagnetic insulator placed on top of the TI) and the TI is a three-dimensional topological insulator of which we consider the top surface, creating a 2D junction. Throughout this paper, the interface normal is along the  $x$  axis and we use periodic

boundary conditions along  $y$ . We assume the junction length to be smaller than the coherence length and the elastic mean free path, making the transport coherent and ballistic.

Quasiparticles undergo normal (Andreev) reflection at the TI/MTI (S/TI) interface. In the MTI/TI/S junction in Fig. 1(c), we consider an incoming electron with the angle  $\theta$  consecutively undergoing Andreev ( $r_{eh}$ ), normal ( $r_{hh}$ ), Andreev ( $r_{he}$ ), and normal ( $r_{ee}$ ) reflection. Figure 1(b) shows the equivalent process in the other half-junction. To generalize the reflection processes and incorporate phase differences due to topology and/or magnetism, we introduce the so-called reflection asymmetry phase  $e^{i\chi} := r_{hh}/r_{ee}^*$  as the ratio between the hole-hole and electron-electron reflection coefficients of the MTI. We compute  $r_{hh}$  and  $r_{ee}$ , by imposing the continuity of the wave function across the junction. The spinor part of the wave function is derived from the Bogoliubov–De Gennes Hamiltonian in the basis  $(\psi_{\uparrow}, \psi_{\downarrow}, \psi_{\downarrow}^{\dagger}, -\psi_{\uparrow}^{\dagger})^T$ ,

$$\hat{H} = \begin{bmatrix} \hat{h}(\mathbf{k}) & \hat{\Delta} \\ \hat{\Delta}^* & -\sigma_y \hat{h}^*(-\mathbf{k}) \sigma_y \end{bmatrix}, \quad (1)$$

where  $\hat{h}(\mathbf{k}) = v_F \hbar \mathbf{k} \cdot \vec{\sigma} + \sigma_z m_z - \mu_j \sigma_0$  is the single-particle Hamiltonian, with  $v_F$  being the Fermi velocity,  $\mathbf{k}$  the momentum vector,  $\vec{\sigma} = (\sigma_x, \sigma_y, \sigma_z)$  the Pauli-matrix vector,  $\mu_j$  with  $j = \text{S, TI, MTI}$  the chemical potential in the three regions,  $m_z$  the induced magnetic gap, and  $\sigma_0$  the  $2 \times 2$  identity matrix.  $\hat{\Delta} = \sigma_0 \Delta_0$ , with  $\Delta_0 \in \mathbb{R}$  is the  $s$ -wave superconducting gap.  $\Delta_0$  and  $m_z$  are only nonzero in their respective regions.

## III. TOPOLOGICAL INVARIANT

The Hamiltonian (1) obeys particle-hole symmetry. In the absence of a magnetic barrier ( $m_z = 0$ ), it is also time-reversal symmetric. This means that the system is placed in the symmetry class BDI when both particle-hole and time-reversal symmetry are present, while it is in class D when time-reversal symmetry is broken [21]. Based on the system's symmetries, the topological invariant  $Q$  (the number of symmetry-protected edge states present at the Fermi level) per spatial dimension can be calculated through the reflection block of the scattering matrix [22] for the TI/MTI interface,  $\hat{r} = \text{diag}(r_{ee}, r_{hh}) \equiv \text{diag}(r_{ee}, e^{i\chi} r_{ee}^*)$ . In 2D, the topological invariant is a winding number, given by  $Q^{2\text{D}} = \frac{1}{2\pi i} \int_0^{2\pi} dk \frac{d}{dk} \log(\det \hat{r})$ , where  $\det \hat{r} = e^{i\chi}$  and we integrate over the momentum  $k$ . Details on the symmetry classes and calculation of  $Q^{2\text{D}}$  are provided in Sec. S1 of the Supplemental Material [23].

We compute  $Q$  with and without time-reversal symmetry, i.e., with and without a magnetic barrier. In time-reversal symmetric junctions ( $m_z = 0$ ), we find  $r_{ee}^* = r_{hh}$ , such that  $e^{i\chi} = 1$  and  $Q^{2\text{D}} = 0$ , implying that the system is topologically trivial and there are no edge modes. In the case of broken time-reversal symmetry ( $m_z \neq 0$ ), we obtain  $Q^{2\text{D}} = -1$  ( $Q^{2\text{D}} = +1$ ) for the S/TI/MTI (MTI/TI/S) half-junction. A topological invariant of  $\mp 1$  means that a topologically protected chiral edge mode is present. Importantly, the sign difference of  $Q$  between the two half-junctions indicates opposite chirality (winding direction), as illustrated in the inset of Figs. 1(d) and 1(e). The protected chiral edge mode in 2D is the nonzero energy chiral Majorana mode originating from

the localized zero-energy Majorana bound state present in the 1D channel at the symmetry point  $\theta = 0$ .

#### IV. CHIRAL MAJORANA MODES

Chiral Majorana modes have been predicted in MTI/S junctions [15], and their bound-state energies  $E_{\text{ABS}}(\theta)$  were previously found as poles in the conduction [24]. We compute  $E_{\text{ABS}}(\theta)$  as the energy  $E$  when the Bohr-Sommerfeld quantization condition  $\alpha_{r_{ee}} + \alpha_{r_{eh}} + \alpha_{r_{hh}} + \alpha_{r_{ne}} = 2\pi n$ ,  $n \in \mathbb{Z}$ , is satisfied for the reflection coefficients depicted in Figs. 1(b) and 1(c). For subgap energies  $|E| < \Delta_0$ , the quantization condition can be written in terms of  $\chi$  as  $-2 \arccos(E/\Delta_0) + \chi = 2\pi n$  (Sec. S2 of the Supplemental Material [23]). Since  $2 \arccos(E/\Delta_0)$  is bound between 0 and  $2\pi$ , the condition is met for a nonzero  $\chi$ . So, the value of  $\chi$  dictates whether ABSs exist. In time-reversal symmetric systems ( $m_z = 0$ ),  $\chi = 0$  and no ABS forms. Whereas in time-reversal symmetry-breaking systems,  $\chi$  is nonzero. The bound-state energies vs incident angle for magnetic S/TI/MTI and MTI/TI/S junctions are shown in Figs. 1(d) and 1(e). At  $\theta = 0$  (i.e., the 1D limit), the ABS is located at zero energy and is therefore a Majorana bound state. For nonzero angles, the ABS moves away from zero energy and obtains a chirality. We recall that the two half-junctions have opposite chirality ( $Q = \mp 1$ ), which results in the  $E_{\text{ABS}}$  having a different sign for a fixed nonzero value of  $\theta$ . Crucially, this means that in the coupled S/TI/MTI/TI/S junction, for a fixed  $\theta$ , there are bound states of opposite energy on the left and right sides of the MTI barrier.

#### V. MULTIPLE ANDREEV REFLECTIONS

To consider the transport in the S/TI/MTI/TI/S junction, we construct the left and right moving wave functions in the two TI regions, as eigenfunctions of Eq. (1). The wave functions live in two-dimensional space  $(x, y)$  and time dimension  $t$ . We assume translational symmetry along  $y$ , and therefore, the  $y$  component of the wave function is the propagating wave  $e^{ik_y y}$ , with  $k_y$  being the momentum in the  $y$  direction. The  $x$  component contains a weighted sum over all moving quasiparticles, where the weights represent the reflection and transmission probabilities.

We consider an incoming electronlike quasiparticle from the left TI with amplitude  $J$ . We define  $n$  as the number of the Andreev reflections. At the MTI, the quasiparticle is either transmitted (amplitude  $C_n$ ) or reflected (amplitude  $B_n$ ).

If this electronlike quasiparticle is transmitted, it reaches the TI/S interface on the right side and is Andreev reflected as a hole with amplitude  $a_1 C_0$ , where  $a_n$  is the Andreev amplitude. We consider a potential difference  $eV$  in the MTI region, such that in the MAR picture [19,20], every time an electron passes from left to right, crossing the MTI, its energy increases by  $eV$ , while the hole energy increases when it passes in the opposite direction. The Andreev reflection coefficient  $a_n$  changes accordingly to  $a_n \equiv r_{eh}(E + neV)$ . We note that the choice of basis results in equal Andreev reflection coefficients  $a_n$  at the left and right S interface [25], which is crucial for the MAR calculations.

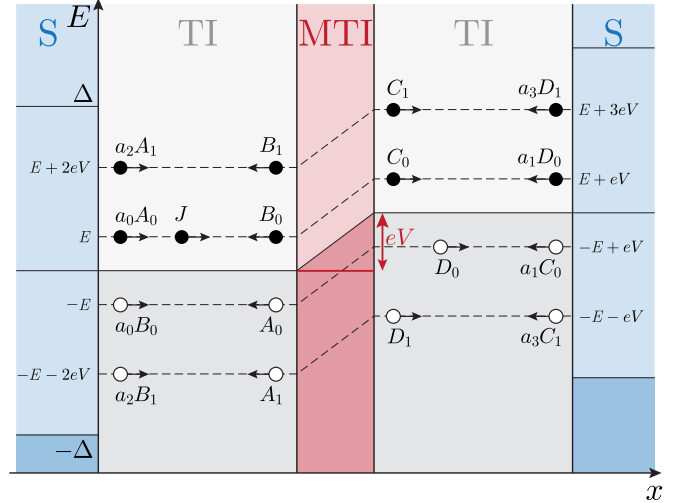


FIG. 2. Schematic illustration of the S/TI/MTI/TI/S junction which illustrates the  $A_n$ ,  $B_n$ ,  $C_n$ , and  $D_n$  reflection and transmission coefficients.  $J$  is the incoming particle in the left TI and  $eV$  is the potential difference contained in the MTI.

If the quasiparticle is instead reflected, it reaches the S/TI interface on the left side and is Andreev reflected with amplitude  $a_0 B_0$ . The holelike quasiparticle at the MTI is either reflected or transmitted with amplitude  $A_n$  or  $D_n$  (depending on which side it comes from) and the process repeats itself. The reflection and transmission processes and the corresponding coefficients are illustrated in Fig. 2.

The time component of the wave function contains the quasiparticle energy. If the quasiparticle is in the left TI region, it has passed MTI an even number of times and its energy is  $\varepsilon + neV$ . If it is in the right TI region, it has gone through MTI an odd number of times and its energy is  $\varepsilon + (2n + 1)eV$ .

In the left TI region, the electron and hole wave functions are  $\psi_{e,h}(x, y, t) = \psi(x) e^{ik_y y} e^{-i(\varepsilon + 2neV)t/\hbar}$ , with [19]

$$\psi_e(x) = \sum_n (a_{2n} A_n + J \delta_{n0}) e^{ik_x x} + B_n e^{-ik_x x},$$

$$\psi_h(x) = \sum_n A_n e^{ik_x x} + a_{2n} B_n e^{-ik_x x},$$

where  $k_x$  is the momentum in the  $x$  direction.

Similarly, in the right TI region, the wave functions are  $\psi_{e,h}(x, y, t) = \psi_{e,h}(x) e^{ik_y y} e^{-i(\varepsilon + (2n+1)eV)t/\hbar}$ , with

$$\psi_e(x) = \sum_n C_n e^{ik_x x} + a_{2n+1} D_n e^{-ik_x x},$$

$$\psi_h(x) = \sum_n a_{2n+1} C_n e^{ik_x x} + D_n e^{-ik_x x}.$$

The MTI is a scattering region that is governed by the scattering matrices for electrons and holes (Sec. S3 of the Supplemental Material [23]):

$$S_e = \begin{bmatrix} r & t \\ t & -\frac{r^* t}{t^*} \end{bmatrix}, \quad S_h = \begin{bmatrix} e^{i\chi} r^* & t^* \\ t^* & -e^{-i\chi} \frac{r t^*}{t} \end{bmatrix}, \quad (2)$$

where  $r \equiv r_{ee}$  and  $t \equiv t_{ee}$  are the electron-electron reflection and transmission coefficients for the MTI barrier and we used  $r_{hh}/r_{ee}^* = e^{i\chi}$ . Two known limits of the scattering matrices are  $e^{i\chi} = 1$  for an S/N/S junction [19] and  $e^{i\chi} = -1$  for a 1D ferromagnetic S/TI/MTI/TI/S junction [20].

The wave functions in the two TI regions are coupled by the scattering matrices (2) as follows:

$$\begin{bmatrix} B_n \\ C_n \end{bmatrix} = S_e \begin{bmatrix} \delta_{n0} + a_{2n}A_n \\ a_{2n+1}D_n \end{bmatrix}, \quad \begin{bmatrix} A_n \\ D_{n-1} \end{bmatrix} = S_h \begin{bmatrix} a_{2n}B_n \\ a_{2n-1}C_{n-1} \end{bmatrix}.$$

The vector on the left contains the quasiparticles outgoing from MTI. The vector on the right represents the quasiparticles incident to MTI. From these matrix equations, we obtain a system of equations with four unknowns,  $A_n$ ,  $B_n$ ,  $C_n$ , and  $D_n$ :

$$\begin{aligned} B_n &= r[\delta_{n0} + a_{2n}A_n] + t a_{2n+1}D_n, \\ C_n &= t[\delta_{n0} + a_{2n}A_n] - \frac{r^*t}{t^*} a_{2n+1}D_n, \\ A_n &= e^{i\chi} r^* a_{2n}B_n + t^* a_{2n-1}C_{n-1}, \\ D_{n-1} &= t^* a_{2n}B_n - e^{-i\chi} \frac{r t^*}{t} a_{2n-1}C_{n-1}. \end{aligned}$$

We substitute these equations into each other to find a single recurrence relation for  $B_n$  (details can be found in Sec. S3 of the Supplemental Material [23]):

$$B_{n+1} + \gamma_n B_n + \chi_n B_{n-1} = \zeta_n \delta_{n0}, \quad (3)$$

with

$$\begin{aligned} \gamma_n &= -\frac{1}{D} \frac{(1 - e^{i\chi} a_{2n}^2)(1 - e^{-i\chi} a_{2n+1}^2)}{a_{2n+1}a_{2n+2}} \\ &\quad - \frac{e^{i\chi} a_{2n}^2}{1 - e^{-i\chi} a_{2n-1}^2} \frac{1 - e^{-i\chi} a_{2n+1}^2}{a_{2n+1}a_{2n+2}} \\ &\quad - e^{-i\chi} \frac{a_{2n+1}}{a_{2n+2}}, \\ \chi_n &= \frac{a_{2n}a_{2n-1}(1 - e^{-i\chi} a_{2n+1}^2)}{a_{2n+1}a_{2n+2}(1 - e^{-i\chi} a_{2n-1}^2)}, \\ \zeta_n &= \frac{r}{D} \frac{1 - e^{-i\chi} a_{2n+1}^2}{a_{2n+1}a_{2n+2}}, \end{aligned}$$

and  $D \equiv tt^* = 1 - rr^*$  is the barrier transparency. The recurrence relation (3) is solved numerically using forward elimination by backward substitution [26]. We use  $B_n$  to express  $A_n$  as

$$A_{n+1} + \gamma'_n A_n = f(n), \quad (4)$$

with  $\gamma'_n = -a_{2n+1}a_{2n}$  and  $f(n) = r^*(e^{i\chi} a_{2n+2}B_{n+1} - a_{2n+1}B_n) + a_1\delta_{n0}$ .

The time dependency of the wave functions  $\psi_{e,h}(x, y, t)$  implies that the current  $I(t)$  oscillates with the Josephson frequency  $\omega_J = 2eV/\hbar$ . Therefore, it is expanded in the Fourier components  $I(eV, t) = \sum_l I_l(eV) e^{il\omega_J t}$ , where the components  $I_l(eV)$  are obtained by averaging over the incident angle,

$$I_l(eV) = \frac{1}{\pi} \int_{-\pi/2}^{\pi/2} I_l(eV, \theta) \cos(\theta) d\theta,$$

where  $l$  is the order of the current. In this work, we consider the DC current, which is found by setting  $l = 0$ . Higher-order currents, such as the AC current, can be obtained by using  $l > 0$ . The angle-dependent components  $I_l(eV, \theta)$  are calculated in terms of  $A_n$  and  $B_n$  [19]. Simplifying the expression at zero temperature, we find

$$I_{\text{DC}}(eV, \theta) = \frac{e}{\pi\hbar} \left[ eV - \int \frac{J^2}{D} \left( a_0^* A_0^* + a_0 A_0 + \sum_n (1 + |a_{2n}|^2)(|A_n|^2 - |B_n|^2) \right) d\varepsilon \right],$$

where the source term  $J$  is taken as  $J = \sqrt{1 - a_0^2}$ .

## VI. ASYMMETRIC $I(V)$ CURVES

First, we investigate the angle-resolved MAR spectra for a 2D S/TI/MTI/TI/S Josephson junction (Fig. 3). In a trivial junction (e.g., S/N/S), there are no states inside the gap, electrons (holes) undergo MARs until they have gained enough energy to leave the gap at  $eV = +(-)2\Delta_0$  [19]. The presence of an ABS in the gap gives rise to extra conduction channels [20]. When the ABS aligns with the ABS on the other side ( $eV = 2E_{\text{ABS}}$ ) [27] or the continuum ( $eV = \Delta_0 + |E_{\text{ABS}}|$ ), additional features appear in the  $I(V)$  curve. Furthermore, due to the nature of MARs, higher-order features appear for successive Andreev reflections. Generally, features in the  $I(V)$  curve are expected at  $eV = (\Delta_0 + |E_{\text{ABS}}|)/n$ , with  $n \in \mathbb{Z}$ , stemming from the alignment of the ABS with the continuum, and at  $eV = 2E_{\text{ABS}}/m$ , for odd  $m \in \mathbb{N}$ , stemming from the alignment of the two ABSs. These alignments are illustrated in Fig. 3. We note that the modes with opposite chirality on the left and right sides of the MTI barrier are retained in the coupled Josephson junction (Sec. S1 of the Supplemental Material [23]). The energy asymmetry resulting from these modes of opposite chirality dictates that  $m$  must be odd. This can be seen by considering an electron initially incoming from the left subgap state. For it to scatter to the empty subgap state on the other side of the barrier it can only traverse the system an odd number of times, gaining an odd multiple of  $eV$  in energy.

The asymmetry of the bound-state energies due to the opposite chirality for the left and right half-junctions in Figs. 1(d) and 1(e) gives rise to the asymmetric  $I(V)$  curve in Fig. 3. For a fixed  $\theta$ , a positive bias voltage  $eV$  aligns levels (associated with higher-order MAR resonances) different than those of a negative bias. In the latter case, the density of states in Figs. 3(c)–3(e) shift in the opposite direction, the  $eV = 2E_{\text{ABS}}$  levels never align, and the associated features in  $I(V)$  are absent for  $eV < 0$ . The  $I(V)$  curve for  $-\theta$  is the vertical mirror image of Fig. 3. The value  $e^{i\chi}$  in the scattering matrices (2) indicates whether ABSs are present;  $e^{i\chi} = 1$  means there are no ABSs and results in a trivial  $I(V)$  curve (meaning no additional subgap features), whereas  $e^{i\chi} = -1$  indicates a nontrivial  $I(V)$  curve with asymmetric peaks, as shown in Fig. 3(a). By changing  $\theta$ , we smoothly transition from the trivial regime to the nontrivial regime [28].

Figure 4 shows the  $I(V)$  spectra of an S/TI/MTI/TI/S junction for positive  $\theta$  ranging from 0 to  $\frac{\pi}{2}$ , with

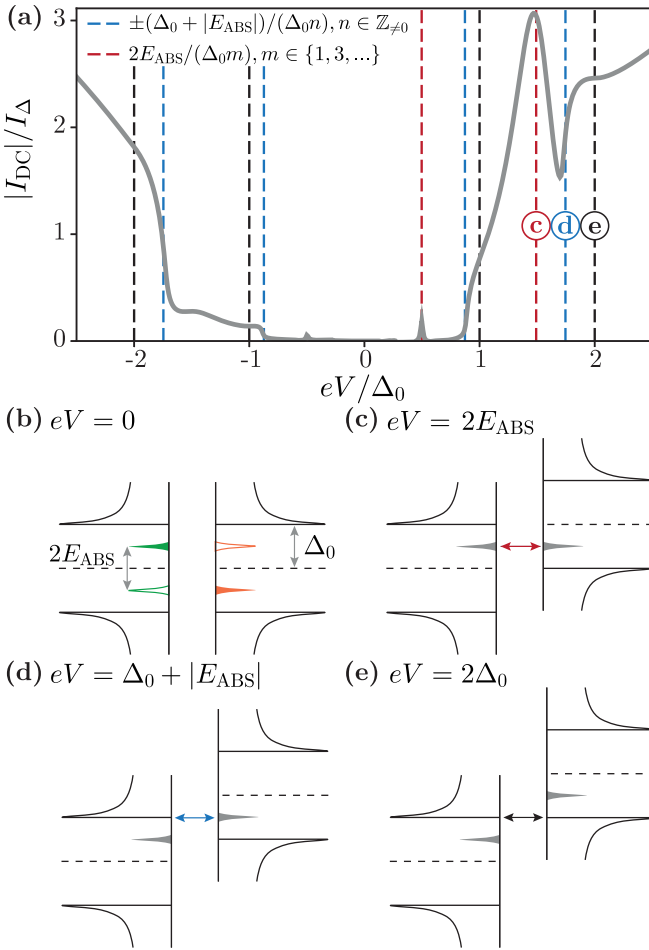


FIG. 3. (a) An asymmetric  $I(V)$  curve of an S/TI/MTI/TI/S junction for a single incident angle  $\theta = 0.45\pi$ , with corresponding  $E_{\text{ABS}}/\Delta_0 = 0.75$ .  $I_{\text{DC}}$  is normalized by  $I_{\Delta} = De\Delta_0/h$ , for the transparency  $D = 0.1$ . The other parameters are  $\mu_{\text{TI}}/m_z \approx 0.7$ , with  $m_z/\Delta_0 = 300$ ,  $\mu_{\text{S}} = \mu_{\text{TI}}$ , and  $\mu_{\text{MTI}} = 0$ , and the MTI barrier width is  $d = 1.5\hbar v_F/m_z$ . (b) The density of states of the two superconductors including the subgap ABSs. The solid (empty) ABS positions correspond to a positive (negative) incident angle. The bias voltage  $eV$  shifts the density of states of the right superconductor relatively upwards. When considering only the solid ABSs for  $\theta > 0$ , transport occurs with the alignment of (c) ABS-ABS, (d) ABS-continuum, and (e) continuum-continuum.

corresponding positive  $E_{\text{ABS}}$  [27]. Two limiting cases are the red curve with the ABS near the continuum ( $E_{\text{ABS}} = \Delta_0$  and  $e^{i\chi} = 1$ ), for which we observe the strong resonance step near  $2\Delta_0$  as in the trivial S/N/S case [19], and the navy curve describing ABS positions in the middle of the gap ( $E_{\text{ABS}} = 0$  and  $e^{i\chi} = -1$ ), for which we obtain the topological 1D S/TI/S limit [20]. The intermediate curves look strikingly different. For negative voltages, there is a gradual transition from one limit to the other, whereas the positive  $eV$ -side features the distinct additional  $2E_{\text{ABS}}/m$  peaks for odd  $m$  due to the asymmetric ABSs. For negative incident angles [ $\theta \in (-\frac{\pi}{2}, 0]$ ], we obtain the vertical mirror image of Fig. 4.

Next we consider the effect of the varying barrier transparency  $D$  on the  $I(V)$  curves. The barrier transparency, defined as  $D = 1 - rr^*$ , scales exponentially with the MTI

width  $d$ . Since  $e^{i\chi}$  is independent of  $d$ , we can probe the effect of  $D$  on the MAR spectra for a fixed  $E_{\text{ABS}}$  (see Fig. 5). A more transparent interface ( $D \gtrsim 0.1$ ) results in broad  $2E_{\text{ABS}}/m$  peaks and spread-out  $(E_{\text{ABS}} + \Delta_0)/n$  steps in  $I(V)$ , and the enhanced transparency obscures any possible signatures of the ABSs coupling. The results for intermediate transparencies ( $0.1 \gtrsim D \gtrsim 10^{-2}$ ) are as in Fig. 4. In the low-transparency limit ( $D \lesssim 10^{-2}$ ), the features in  $I(V)$  become sharp, resembling a tunnel barrier [29]. Subtle features in the normalized current are enhanced for low  $D$ , and previously suppressed resonance features at  $-2E_{\text{ABS}}/m$  now become visible (at  $eV/\Delta_0 = 2 \times 0.7 = 1.4$  in Fig. 5). These features are an indication of avoided level crossing relating to the overlap between the left and right bound states. The effect is most pronounced at low  $E_{\text{ABS}}$ , and when the bound states move away from the middle of the gap ( $|E_{\text{ABS}}| > 0$ ), the overlap quickly diminishes (see Sec. S4 of the Supplemental Material [23]). Since the observed signatures of coupling are weak, we can primarily explain the features in the reported  $I(V)$  curves (Figs. 3 and 4) by two isolated chiral Majorana modes.

## VII. NANOWIRES AND LATERAL JUNCTIONS

We now consider the consequences of the presence of ABSs and their effect on the  $I(V)$  spectra in realistic experimental setups. A system that the MAR scheme can be readily applied to is topological nanowires [30–33]. We consider a cylindrical geometry with periodic boundary conditions, where, due to the confinement, we obtain a set of allowed quantized  $k_y$  values. Throughout this work, we assumed an infinite junction in the  $y$  direction, meaning that there is a continuum of  $k_y$  channels and every incident angle  $\theta$  is allowed. In the nanowire picture, only the  $\theta$  and  $-\theta$  channels per confined  $k_y$  value are present, and we estimate the current through the nanowire by  $\sim I(\theta) + I(-\theta)$ . The subgap resonances at  $eV = 2E_{\text{ABS}}$ , which are a signature of the asymmetric chiral Majorana modes, are retained in the nanowire (see the inset of Fig. 4).

In 2D samples (lateral junctions on thin films), one generally measures the angle-averaged  $I(V)$  and the asymmetric features disappear (see the black dashed line in Fig. 4). To probe the proposed angle asymmetry, specialized setups for measuring Andreev-reflection angles are required; patterned TI nanostructures offer such capabilities [34]. The caveat is that the conservation of  $k_y$  is an assumption to the current proposal, but in any experimental setup, the junction is finite in the  $y$  direction. Experimental realizations should target a small selection of angles to probe the asymmetry, while sufficiently conserving  $k_y$  over a length scale of typically the coherence length. A natural experimental starting point could be placing (one of) the S leads or the MTI under an angle. Testing potential experimental geometries is an interesting and nontrivial problem, but it is beyond the scope of this work.

## VIII. WIDER APPLICATIONS

The proposed MAR scheme can be applied to nontopological Josephson junctions as well. Subgap states are present in any  $s$ -wave Josephson junction with broken time-reversal symmetry, but the (a)symmetric nature of the ABSs is not

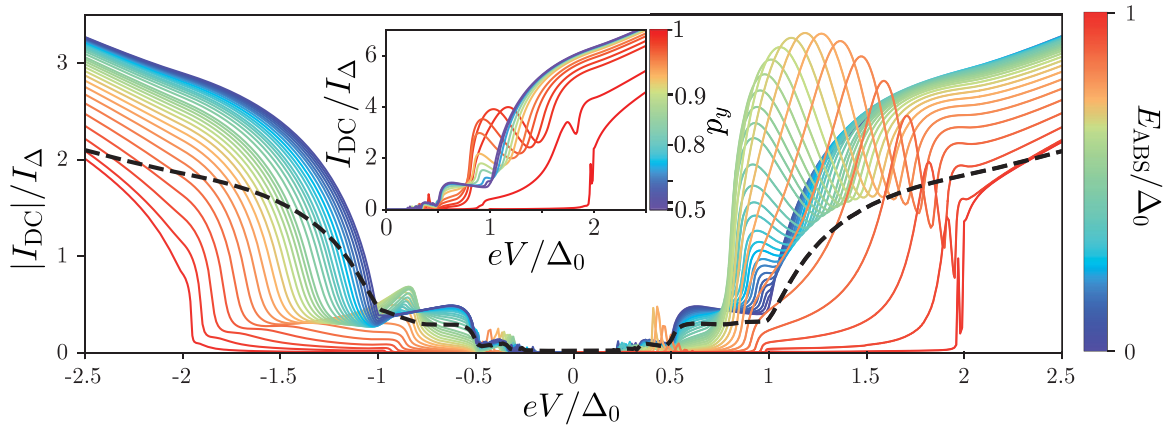


FIG. 4. The angle-resolved asymmetric  $I(V)$  curves for an S/TI/MTI/TI/S junction normalized by  $I_\Delta = De\Delta_0/h$ . Each curve corresponds to a single incident angle  $\theta \in (0, \pi/2)$ , with corresponding bound-state energy  $E_{\text{ABS}}(\theta)$ . The black dashed line is the angle average obtained in the lateral 2D junction limit. The parameters are  $\mu_{\text{TI}}/m_z \approx 0.7$ , with  $m_z/\Delta_0 = 300$ ,  $\mu_S = \mu_{\text{TI}}$ , and  $\mu_{\text{MTI}} = 0$ . The transparency ranges from  $D = 0.05$ – $0.2$ , and the MTI barrier width is  $d = 1.5\hbar v_F/m_z$ . Inset: Nanowire limit. Each  $I(V)$  curve corresponds to a single (normalized) quantized  $p_y = \sin\theta$  channel where the current is estimated by  $I(-\theta) + I(\theta)$ . The graph is identical for  $\pm eV/\Delta_0$ .

universal. For instance, in ferromagnetic Josephson junctions [7–9] the ABSs are degenerate (on both sides of the barrier), no energy asymmetry is present, and the  $I(V)$  curves are symmetric.

An asymmetry in the  $I(V)$  curves is, however, not unique to topological junctions. In fact, any non-centrosymmetric system with broken time-reversal symmetry features nonreciprocal (asymmetric) responses [35]. In the S/TI/MTI/TI/S system under consideration, the presence of the chiral Majorana modes of opposite chirality on opposite sides of the barrier breaks inversion symmetry (playing the role of non-centrosymmetry), which in combination with the breaking of time-reversal symmetry due to the MTI leads to the asymmetric  $I(V)$ . An interesting extension of the current work would be to apply the MAR scheme to the case of an in-plane magnetization in the MTI [36] and study its effect on the  $I(V)$  spectra.

So far, we have considered different interlayer materials, but the required broken symmetries can also be included in the superconductors. Unconventional superconductors are

characterized by an anisotropic order parameter with a phase—e.g.,  $p_x$  wave as in the Kitaev chain [37] and  $d$ -wave high- $T_c$  cuprates [11,12]. Unconventional superconductors can have a range of exotic properties such as intrinsic chirality, which ensures the existence of chiral bound states, or intrinsically broken time-reversal symmetry, which eliminates the need for a magnetic barrier.

To implement unconventional superconductivity in our model, we recall that the choice of basis is crucial to get equal Andreev reflection coefficients  $a_n$  at the left and right S interfaces. One can construct a unitary transformation to transfer the phase from the order parameter to  $e^{i\chi}$  such that  $a_n$  remains equal at both S interfaces and the MAR scheme is still valid (see Sec. S5 of the Supplemental Material [23] for details).

## IX. CONCLUSIONS

In conclusion, we have investigated the emergence of ABSs in 2D topological magnetic Josephson junctions and studied their effect on calculated  $I(V)$  spectra. When an ABS on one side of the junction aligns with an ABS on the other side or with the continuum, a conduction channel opens which appears as a peak in the  $I(V)$  curve. This directly links the  $I(V)$  curve to the ABS energies.

Due to the nature of the TI, a single topologically protected ABS is present at both MTI interfaces, which obtains a chirality (winding number) in 2D. The S/TI/MTI/TI/S junction features bound states of opposite chirality on either side of the MTI barrier and the corresponding bound-state energies are inverted. This energy asymmetry is responsible for the asymmetric  $I(V)$  curve. We have investigated two limits of the S/TI/MTI/TI/S  $I(V)$  curve. In the nanowire limit, the distinct peaks, which are an artifact of the present asymmetric chiral Majorana modes, are robust for quantized  $k_y$  channels. In lateral 2D junctions where one experimentally obtains an angle-averaged  $I(V)$  curve, the asymmetry disappears but nontrivial steps related to the presence of subgap states remain.

The concept of nonreciprocity has regained interest in the field of superconductivity as a potential probe for broken

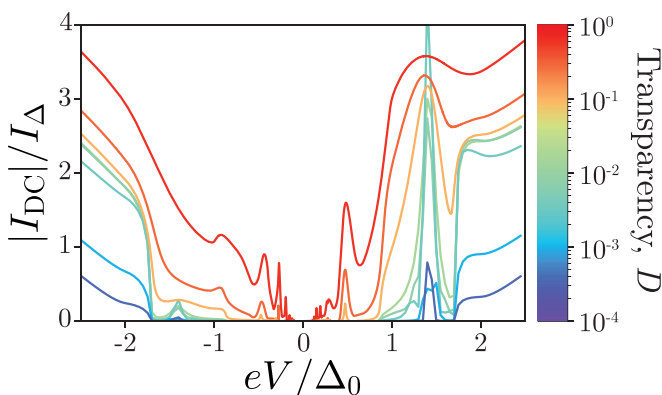


FIG. 5. Effect of increasing transparency  $D$  on the MAR  $I(V)$  spectra for  $E_{\text{ABS}}/\Delta_0 = 0.7$ . The parameters are  $\mu_{\text{TI}}/m_z \approx 0.5$ , with  $m_z/\Delta_0 = 300$ ,  $\mu_S = \mu_{\text{TI}}$ , and  $d \approx 3.3\hbar v_F/m_z$ .

symmetries [35]. In the S/TI/MTI/TI/S case, the nonreciprocity arises from the energy asymmetry as a function of  $\theta$  between the two emergent bound states of opposite chirality on either end of the MTI barrier. Particle-hole symmetry is not violated in this case since the energy of the subgap state also inverts as  $\theta$  is inverted. We propose angle-resolved ABS spectroscopy to resolve the predicted asymmetry.

#### ACKNOWLEDGMENTS

L.A.B.O.O. and J.W.A.R. were supported by the EPSRC through the Core-to-Core International Network “Oxide

Superspin” (Grant No. EP/P026311/1) and a “Superconducting Spintronics” Programme Grant (Grant No. EP/N017242/1). L.A.B.O.O. also acknowledges support from a Doctoral Training Partnership Grant (Grant No. EP/N509620/1). S.R.D.W. is supported by the European Union’s Horizon 2020 research and innovation programme (Grant No. 862046). S.-I.S. is supported by a JSPS Postdoctoral Fellowship for Overseas Researchers and a Grant-in-Aid for JSPS Fellows (JSPS KAKENHI Grant No. JP19J02005). We acknowledge useful discussions with Alexander Golubov.

- 
- [1] A. F. Andreev, *Sov. Phys. JETP* **19**, 1228 (1964).  
 [2] I. O. Kulik, *Sov. Phys. JETP* **30**, 944 (1970).  
 [3] Yu Luh, *Acta Phys. Sin.* **21**, 75 (1965).  
 [4] H. Shiba, *Prog. Theor. Phys.* **40**, 435 (1968).  
 [5] A. Rusinov, *JETP Lett.* **9**, 146 (1969).  
 [6] C. Caroli, P. De Gennes, and J. Matricon, *Phys. Lett.* **9**, 307 (1964).  
 [7] M. Eschrig, *Philos. Trans. R. Soc., A* **376**, 20150149 (2018).  
 [8] D. Beckmann, F. Hübler, M. J. Wolf, and H. v. Löhneysen, *Philos. Trans. R. Soc., A* **376**, 20150002 (2018).  
 [9] M. Eschrig, J. Kopu, J. C. Cuevas, and G. Schön, *Phys. Rev. Lett.* **90**, 137003 (2003).  
 [10] C.-R. Hu, *Phys. Rev. Lett.* **72**, 1526 (1994).  
 [11] Y. Tanaka and S. Kashiwaya, *Phys. Rev. Lett.* **74**, 3451 (1995).  
 [12] S. Kashiwaya and Y. Tanaka, *Rep. Prog. Phys.* **63**, 1641 (2000).  
 [13] N. Read and D. Green, *Phys. Rev. B* **61**, 10267 (2000).  
 [14] C. W. J. Beenakker, *Annu. Rev. Condens. Matter Phys.* **4**, 113 (2013).  
 [15] L. Fu and C. L. Kane, *Phys. Rev. Lett.* **100**, 096407 (2008).  
 [16] V. Mourik, K. Zuo, S. M. Frolov, S. R. Plissard, E. P. A. M. Bakkers, and L. P. Kouwenhoven, *Science* **336**, 1003 (2012).  
 [17] Y. Tanaka, S. Kashiwaya, and T. Yokoyama, *Phys. Rev. B* **71**, 094513 (2005).  
 [18] K. T. Law, P. A. Lee, and T. K. Ng, *Phys. Rev. Lett.* **103**, 237001 (2009).  
 [19] D. Averin and A. Bardas, *Phys. Rev. Lett.* **75**, 1831 (1995).  
 [20] D. M. Badiane, M. Houzet, and J. S. Meyer, *Phys. Rev. Lett.* **107**, 177002 (2011).  
 [21] S. Ryu, A. P. Schnyder, A. Furusaki, and A. W. W. Ludwig, *New J. Phys.* **12**, 065010 (2010).  
 [22] I. C. Fulga, F. Hassler, and A. R. Akhmerov, *Phys. Rev. B* **85**, 165409 (2012).  
 [23] See Supplemental Material at <http://link.aps.org/supplemental/10.1103/PhysRevB.107.184510> for derivations and details of the model.  
 [24] Y. Tanaka, T. Yokoyama, and N. Nagaosa, *Phys. Rev. Lett.* **103**, 107002 (2009).  
 [25] In our chosen basis,  $a_n$  is equal to the reflection coefficients  $r_{eh} = r_{he} = (E - \sqrt{E^2 - \Delta_0^2})/\Delta_0$ ; see Sec. S2 of the Supplemental Material [23].  
 [26] W. Gautschi, *SIAM Rev.* **9**, 24 (1967).  
 [27] The bound-state energy  $E_{\text{ABS}}$  is defined in the S/TI/MTI half-junction. In the full S/TI/MTI/TI/S junction,  $E_{\text{ABS}}$  is positive for  $\theta > 0$ .  
 [28] The value at which the transition happens depends on the barrier strength  $\mu_{\text{TI}}/m_z$ . In the strong barrier limit (low  $\mu_{\text{TI}}/m_z$ ), the system resembles two mostly isolated half-junctions with a large nontrivial regime, whereas for a weak barrier the nontrivial regime is confined to  $\theta = 0$ .  
 [29] G. E. Blonder, M. Tinkham, and T. M. Klapwijk, *Phys. Rev. B* **25**, 4515 (1982).  
 [30] F. Xiu, L. He, Y. Wang, L. Cheng, L.-T. Chang, M. Lang, G. Huang, X. Kou, Y. Zhou, X. Jiang, Z. Chen, J. Zou, A. Shailos, and K. L. Wang, *Nat. Nanotechnol.* **6**, 216 (2011).  
 [31] A. M. Cook, M. M. Vazifeh, and M. Franz, *Phys. Rev. B* **86**, 155431 (2012).  
 [32] Y. C. Arango, L. Huang, C. Chen, J. Avila, M. C. Asensio, D. Grützmacher, H. Lüth, J. G. Lu, and T. Schäpers, *Sci. Rep.* **6**, 29493 (2016).  
 [33] D. Rosenbach, T. W. Schmitt, P. Schüffelgen, M. P. Stehno, C. Li, M. Schlenvoigt, A. R. Jalil, G. Mussler, E. Neumann, S. Trellenkamp, A. A. Golubov, A. Brinkman, D. Grützmacher, and T. Schäpers, *Sci. Adv.* **7**, eabf1854 (2021).  
 [34] K. Moors, P. Schüffelgen, D. Rosenbach, T. Schmitt, T. Schäpers, and T. L. Schmidt, *Phys. Rev. B* **97**, 245429 (2018).  
 [35] Y. Tokura and N. Nagaosa, *Nat. Commun.* **9**, 3740 (2018).  
 [36] O. Maistrenko, B. Scharf, D. Manske, and E. M. Hankiewicz, *Physical Review B* **103**, 054508 (2021).  
 [37] A. Y. Kitaev, *Phys.-Usp.* **44**, 131 (2001).